

Rotating Bullets from A Variable Protostar

Xuepeng Chen¹, Héctor G. Arce², Qizhou Zhang³, Ralf Launhardt⁴, and Thomas Henning⁴

¹*Purple Mountain Observatory, Chinese Academy of Sciences, 2 West Beijing Road, Nanjing 210008, China; xpchen@pmo.ac.cn*

²*Department of Astronomy, Yale University, Box 208101, New Haven, CT 06520-8101, USA*

³*Harvard-Smithsonian Center for Astrophysics, 60 Garden Street., Cambridge, MA 02138, USA*

⁴*Max Planck Institute for Astronomy, Königstuhl 17, D-69117 Heidelberg, Germany*

ABSTRACT

We present SMA CO (2–1) observations toward the protostellar jet driven by SVS 13 A, a variable protostar in the NGC 1333 star-forming region. The SMA CO (2–1) images show an extremely high-velocity jet composed of a series of molecular “bullets”. Based on the SMA CO observations, we discover clear and large systematic velocity gradients, perpendicular to the jet axis, in the blueshifted and redshifted bullets. After discussing several alternative interpretations, such as twin-jets, jet precession, warped disk, and internal helical shock, we suggest that the systematic velocity gradients observed in the bullets result from the rotation of the SVS 13 A jet. From the SMA CO images, the measured rotation velocities are 11.7–13.7 km s^{−1} for the blueshifted bullet and 4.7 ± 0.5 km s^{−1} for the redshifted bullet. The estimated specific angular momenta of the two bullets are comparable to those of dense cores, about 10 times larger than those of protostellar envelopes, and about 20 times larger than those of circumstellar disks. If the velocity gradients are due to the rotation of the SVS 13 A jet, the significant amount of specific angular momenta of the bullets indicates that the rotation of jets/outflows is a key mechanism to resolve the so-called “angular momentum problem” in the field of star formation. The kinematics of the bullets suggests that the jet launching footprint on the disk has a radius of ~ 7.2 – 7.7 au, which appears to support the extended disk-wind model. We note that further observations are needed to comprehensively understand the kinematics of the SVS 13 A jet, in order to confirm the rotation nature of the bullets.

Subject headings: binaries: general — ISM: individual objects (NGC 1333 SVS 13) — ISM: jets and outflows — stars: formation

1. INTRODUCTION

Stars form from the gravitational collapse of dense cores in molecular clouds. It has been long recognized that in the star formation process specific angular momenta need to be reduced by 6–7 orders of magnitude from a dense core to a typical main-sequence star, like the Sun. This puzzle has been regarded as the “angular momentum problem” in the field of star formation (e.g., Spitzer 1978; Bodenheimer 1995). Obviously, the extraction of excess angular momentum is essential in the star formation process.

In the early phase of star formation, when a young stellar object (YSO) accretes mass from its surrounding disk, it also ejects mass in a bipolar jet. The ejected material can accelerate entrained gas to velocities larger than those of the cloud, thereby creating a molecular outflow. Numerous observations indicate that most, if not all, stars drive accretion-powered jets and outflows during their formation (Reipurth & Bally 2001; Arce et al. 2007). The jets are believed to be driven by rotating disks through magneto-centrifugal processes, although the precise origin of jets from YSOs is still in debate (Blandford & Payne 1982; Pudritz et al. 2007; Shang et al. 2007). The rotation of jets and outflows about their symmetry axis is widely considered to be a key mechanism to remove angular momentum from forming protostars, and thus, at least partially, to solve the angular momentum problem in star formation. Furthermore, rotational kinematics of jets and outflows can be used to study jet-launching mechanism and to discriminate different jet-launching theories (Frank et al. 2014).

As a consequence, many groups have searched for rotation signatures in jets and outflows, i.e., radial velocity gradients or shifts across the axes of jets/outflows. However, the detection of jet/outflow rotation is extremely difficult, as both high angular and spectral resolution are required (see, e.g., Ray et al. 2007). As shown by Pesenti et al. (2004), the underlying rotation signature of jets/outflows could be easily diluted and made undetectable in low angular resolution observations. During the past two decades, radial velocity gradients/shifts have been observed in a small number of jets and molecular outflows (see reviews by Bachiotti et al. 2009; Belloche 2013; Frank et al. 2014). However, several alternative interpretations other than rotation have been suggested to explain the observed velocity gradients/shifts across jets/outflows, such as asymmetric shocking against a warped disk (Soker 2005), jet precession (e.g., Cerqueira et al. 2006), helical MHD shocks (Fendt 2011), and twin-jets (Soker & McIcley 2013). Hence, one must be cautious when interpreting observed velocity gradients across jet/outflows. As suggested by Belloche (2013), the following requirements are needed to convincingly detect rotation in jets or outflows. First of all, the kinematic signature, a velocity gradient perpendicular to the jet axis, has to be consistent all along the jet length. Second, the signature should be consistent between both lobes and

with the disk rotation. Finally, the velocity profile should be spectrally resolved. Taking these requirements into account reduces the number of candidate rotating jets/outflows to less than 10.

A widely accepted prototypical example of such rotational jets/outflows is DG Tau, a small jet driven by a Class II T Tauri star. High angular resolution HST observations revealed in the DG Tau jet a large velocity shift across the jet axis ($\sim 20 \text{ km s}^{-1}$), which is consistent with the rotation direction of the circumstellar disk (Bachioti et al. 2002). Another promising candidate is the molecular outflow in CB 26, driven by an isolated T Tauri star (Launhardt et al. 2009). As calculated by Launhardt et al. (2009), the (specific) angular momentum in the CB 26 circumstellar disk can be extracted by the outflow in a time scale of $\sim 10^6$ years. A few other rotational jet/outflow candidates, e.g., TH 28 and CW Tau (Coffey et al. 2007), show similar rotational signatures in the high angular resolution observations. These jets/outflows are so far the prime candidates for studying jet-driving mechanisms.

Although promising rotation jets/outflow candidates from a few T Tauri stars have been observed, these stellar objects are well past their main accretion/ejection phase. As most of the stellar mass is accreted during the protostellar phases, most of the angular momentum loss must have occurred by then as well, with only a small fraction left to deal with during the T Tauri evolution. In particular, the initial amount of angular momentum, and its evolution and re-distribution appear to be key factors in many of the processes which determine the protostellar fragmentation, the final stellar mass(es), and the existence and morphology of planetary systems. Therefore, it is of prime importance to detect and study rotating jets/outflows from protostars when the removal/evolution of angular momentum is more crucial. In recent years, a few rotational outflow candidates were found in embedded protostars, although none of them have been confirmed (see, e.g., Belloche 2013). In a series of studies toward HH 211, Lee et al. (2009) reported a tentative detection of rotation ($\sim 1.5 \text{ km s}^{-1}$ velocity shift), but the rotation direction is opposite to the gradient direction found by Lee et al. (2007). For the HH 212 outflow, the tentative detection of a rotation velocity shift ($\sim 1.5 \text{ km s}^{-1}$) reported by Lee et al. (2008) is not confirmed by other observations (e.g., Codella et al. 2007; Correia et al. 2009). Zapata et al. (2010b) reported a candidate rotating jet in Ori-S6. However, the driving source of the jet is a close binary system with a separation of ~ 50 au (Zapata et al. 2007), implying that the rotation signature may be explained by the twin-jets scenario. In addition, the referred launching footprint of the Ori-S6 jet, $\sim 140/(\sin i)^{3/4}$ au (where i is the inclination angle of the jet; see Zapata et al. 2010b), is larger than that of the binary separation, not to mention the circumstellar disk in the system. Furthermore, the direction of the velocity gradient across the jet is also opposite to that of the gradient found in the circumbinary ring (Zapata et al. 2010a). The other two protostellar outflows, NGC 1333 IRAS 4A (Choi et al. 2011) and IC 348 MM2 (Pech et

al. 2012), may be also explained by the twin-jets scenario (see Soker & McIey 2013 and Rodríguez et al. 2014, respectively). Therefore, there is no convincing detection of rotating jets/outflows from protostars yet.

In this paper, we report Submillimeter Array¹ (SMA; Ho et al. 2004) CO (2–1) line observations toward the protostellar jet driven by SVS 13 A, a Class 0/I transition protostar located in the Perseus NGC 1333 star-forming region (Bachiller et al. 2000; Chen et al. 2009). The distance of SVS 13 A is accurately determined to be 235 ± 18 pc based on VLBI parallax measurements of masers associated with this object (Hirota et al. 2008). SVS 13 A is well-known for driving an extremely high-velocity CO outflow (see, e.g., Bachiller et al. 1990; Masson et al. 1990), which records the highest velocity CO outflow known thus far. With Very Large Array (VLA) 3.6 cm observations, Anglada et al. (2000) resolved source SVS 13 A into a close binary system, VLA 4A and VLA 4B, with an angular separation of $0''.3$. Further VLA 7 mm observations indicated that only VLA 4B is associated with a circumstellar disk (Anglada et al. 2004). Indeed, high angular resolution near-infrared observations at the Keck telescopes show that VLA 4B is the driving source of the SVS 13 A protostellar jet (Hodapp & Chini 2014).

Another interesting characteristic of SVS 13 A is its variability. After its discovery in infrared observations (Strom et al. 1976), this source experienced a sudden increase in brightness around 1990 (~ 1.5 magnitude changed in the K band; see Hodapp & Chini 2014 and references therein). This phenomenon is traditionally classified as either FU Orionis (FUor) or EX Lupi (EXor) type outbursts, depending on the duration of the outburst and its spectrum (see a recent review by Audard et al. 2014). In both classes, an increase in the accretion rate onto the star is thought to be responsible for the luminosity increase. After analyzing the infrared data collected over the course of the past 24 years, Hodapp & Chini (2014) concluded that the elevated post-outburst level of accretion and, therefore, jet activity in SVS 13 A has persisted for the past two decades. The light curve of SVS 13 A shares the long duration maximum with FUors, while spectroscopically, it resembles an EXor, and the small outburst amplitude resembles neither (see Hodapp & Chini 2014). Therefore, SVS 13 A represents an object somewhere between those two classical cases.

There is growing evidence that protostellar accretion cannot be steady in general, but must alternate between high and low states of accretion (Hartmann & Kenyon 1996; Audard et al. 2014). Both observational and theoretical studies suggest that variable protostellar

¹The Submillimeter Array is a joint project between the Smithsonian Astrophysical Observatory and the Academia Sinica Institute of Astronomy and Astrophysics and is funded by the Smithsonian Institution and the Academia Sinica.

accretion with episodic outbursts may be a standard phenomenon in star formation. A recent discovery of an outbursting Class 0 protostar indicates that episodic accretion occurs already at the very early phase of star formation (Safron et al. 2015), which is consistent with the prediction of theoretical simulations (e.g., Vorobyov & Basu 2015). On the other hand, episodic ejection events seem also to be a common property of protostellar jets and outflows (Reipurth & Bally 2001; Arce et al. 2007). Due to the physical link between accretion and ejection, this could be explained by variations in the accretion rate onto the forming star, which results in variations on the velocity of the ejected matter, hence the creation of a series of shocks. The SVS 13 A jet, also well-known as Herbig-Haro (HH) flow 7-11, comprised of a long chain of individual shock fronts (see, e.g., Raga et al. 2013) and molecular outflow clumps (see, e.g., Plunkett et al. 2013), is a typical example of such protostellar jets. Therefore, the variability of SVS 13 A and its jet structure also provide an important opportunity to study the relationship between episodic accretion and outbursts.

2. OBSERVATIONS AND DATA REDUCTION

The data presented in this work were taken with the Submillimeter Array (Ho et al. 2004), an interferometer array of eight 6-meter antennas at Mauna Kea, Hawaii. We observed SVS 13 at 230 GHz on 2008 December 7th in the SMA compact configuration. Eight antennas were used in the array, providing baselines with projected lengths from ~ 9 to 59 k λ . The receiver was set up to cover the frequency ranges of 219.5–221.3 GHz and 229.5–231.3 GHz in the lower and upper sidebands, respectively. This setup includes three isotopic CO lines of ^{12}CO (2–1) (230.538 GHz), ^{13}CO (2–1) (220.399 GHz), and C^{18}O (2–1) (219.560 GHz), as well as the 1.3 mm dust continuum emission. In the observations, system temperatures of SVS 13 ranged from 130 to 290 K (depending on elevation), with a typical value of ~ 160 K. The SMA primary beam is approximately $55''$ at 230 GHz.

The data were reduced using the IDL MIR package (Qi 2005). During the reduction, visibility points with clearly deviating phases and/or amplitudes were flagged. The passband (spectral response) was calibrated through observations of the strong quasar 3C273. Time variations in amplitude and phase were calibrated through frequent observations of quasars 0238+166 and 0359+509. Uranus was used for absolute flux calibration, and we estimate a flux accuracy of about 15%.

The calibrated visibility data were then imaged using the MIRIAD toolbox (Sault et al. 1995). The data were imaged by first computing the inverse Fourier transform of the data with the *invert* task. The dirty map was then deconvolved using the CLEAN algorithm with the *clean* task down to 1–2 times the rms noises level. The cleaned components were

then convolved with the clean beam using the *restore* task. With robust uv weighting +1, cleaned maps of the CO (2–1) emission were produced with an effective synthesized beam size of $2''.8 \times 2''.6$. The 1σ rms noise level is $\sim 30\text{--}35$ mJy beam $^{-1}$ at a velocity resolution of ~ 1.0 km s $^{-1}$.

3. RESULTS: SMA CO (2–1) MAPS

In the SMA observations, the CO (2–1) line emission from SVS 13 A is detected in a velocity range from approximately -150 to $+150$ km s $^{-1}$, while the systemic LSR radial velocity of the ambient molecular cloud is about $+9$ km s $^{-1}$ (see Chen et al. 2009). Such a large velocity range of CO emission represents so far the highest velocity molecular outflow detected from a protostar. Following Bachiller et al. (2000), we have divided the high-velocity emission into a limited number of velocity intervals. In this work we focus on the “extremely high velocity” (EHV) components (radial velocities more than 70 km s $^{-1}$ over the cloud systemic velocity), whereas other velocity components will be studied in another work.

Figure 1 shows the velocity-integrated intensity map of the EHV CO (2–1) emission from SVS 13 A, plotted on the SMA 1.3 mm dust continuum image. The CO map shows a high-velocity blueshifted jet, emanating from SVS 13 A towards the southeast. The position angle of the jet is 154 ± 1 degree (measured east from north). This jet consists of three well aligned knots, or so-called “molecular bullets”. The LSR velocities of the three blueshifted bullets are estimated to be -70 , -110 , and -150 km s $^{-1}$, respectively; the three bullets are named blue bullets 1, 2, and 3 (see Figure 1). The projected distance between SVS 13 A and blue bullet 3, the bullet that is the farthest from the driving source, is approximately $22''$ (~ 5200 au at the distance of 235 pc). To the northwest of SVS 13 A and roughly aligned with the blueshifted jet, the EHV redshifted emission shows another bullet, with an LSR velocity of about $+145$ km s $^{-1}$. This redshifted bullet, referred to as red bullet in this work, is $\sim 16''$ (or ~ 3800 au) away from SVS 13 A, spatially coincident with the small redshifted clump “R” found by Bachiller et al. (2000).

Figure 2 shows the intensity-weighted velocity map of the CO (2–1) emission (1st moment map). The images reveal in blue bullet 2 a previously undiscovered systematic velocity gradient, which is perpendicular to the local jet axis (defined by the jet wiggle morphology, see below). A systematic velocity gradient is also revealed in the red bullet, and the direction of the gradient is consistent with that of blue bullet 2, i.e., the left side of the jet axis is blueshifted while the right side is redshifted. The CO velocity channel maps of the blue bullets and red bullet are shown in Appendix (Figures 7 to 9), where detailed kinematic information of the bullets can also be found. On the other hand, as seen in Figure 2, the

velocity field of blue bullet 1 shows a linear gradient along the jet axis, increasing from the driving source SVS 13 A to the southeast. This feature, generally referred to as the “Hubble-law”, is frequently seen in jet-driven outflows (Lada & Fich 1996; Arce & Goodman 2001). It appears that the velocity field of the red bullet is also partially affected by this “Hubble-law” effect in the direction of the jet. The velocity field of blue bullet 3 also shows this “Hubble-law” kinematics (see Figure 2), which will not be further discussed in this work.

Figure 3 shows the position-velocity (PV) diagrams for the two cuts across blue bullet 2 and red bullet (see Figure 2). The PV diagrams also indicate the presence of systematic velocity gradients perpendicular to the jet axis in the two bullets. For blue bullet 2, the velocity shifts (v_{shift}) and shift distances (L_{shift}), measured between the blue and red peaks in the PV diagram (see Fig. 3), are $\sim 15.0\text{--}17.6 \text{ km s}^{-1}$ and $\sim 3''.7\text{--}4''.5$ (depending on cut positions), respectively. For the red bullet, the velocity shift and shift distance are $\sim 5.6 \pm 0.5 \text{ km s}^{-1}$ and $\sim 10''.3 \pm 0''.5$, respectively. At the distance of 235 pc, the derived velocity gradients are $\sim 2.5\text{--}4.1 \times 10^3 \text{ km s}^{-1} \text{ pc}^{-1}$ for blue bullet 2 and $\sim 0.5 \times 10^3 \text{ km s}^{-1} \text{ pc}^{-1}$ for the red bullet. These gradients are about two orders of magnitudes larger than those typically observed in protostellar envelopes (e.g., Belloche et al. 2002; Chen et al. 2007; Tobin et al. 2011).

4. DISCUSSION

4.1. Episodic Ejections of Bullets

As shown in Figure 4, the blueshifted SVS 13 A jet presents a wiggling morphology, which is frequently seen in YSOs jets/outflows, e.g., HH 30 (Anglada et al. 2007) and HH 211 (Lee et al. 2010). This wiggle of the jet is widely thought to be caused by the orbital motion of the jet source in a binary system (see, e.g., Fendt & Zinnecker 1998; Masciadri & Raga 2002). We therefore model the wiggle of the jet using a similar method as described in Lee et al. (2010). In this binary model, the orbit has a period P_o and a radius R_o (the orbital radius of the jet source with respect to the binary center of mass); the ejection velocity of the jet has a component in the orbital plane due to orbital motion, v_o , and a component perpendicular to this orbital plane v_j ; the periodic length is defined as $\Delta z \equiv v_j P_o$ and the velocity ratio as $\kappa \equiv v_o/v_j$.

Figure 4 shows the best fit of this model to the blueshifted jet. As seen in Fig. 4, the wiggle of the jet can be reasonably fitted by this model. This agreement between the observations and model appears to support the scenario that the wiggle of the blueshifted jet results from the orbital motion of the driving source. The best-fit parameters are periodic length $\Delta z = 8''.5 \pm 0''.2$ and $\kappa = 0.075 \pm 0.003$. The parameters of the model are directly

related to the observations: κ is related to the half-opening angle α of the jet cone, $\kappa = \tan \alpha \sin i$, where i is the inclination angle with respect to the line of sight and is adopted as 40° in this work (see, e.g., Davis et al. 2001; Takami et al. 2006). The orbital radius R_o is related to the periodic length Δz of the wiggle,

$$R_o = \frac{\Delta z \tan \alpha}{2\pi}. \quad (1)$$

The derived orbital radius R_o is approximately $0''.16 \pm 0''.02$, which is consistent with the results from the VLA observations (Anglada et al. 2000; 2004).

However, the period of the curve in Figure 4 showing the best-fit model does not precisely match the spacings between the blue peaks. In the SMA CO observations, the spacing between bullets 1 & 2 (~ 2600 au) is different from that between bullets 2 & 3 (~ 2000 au). The proper motions of the SVS 13 A jet have been well studied at optical and near-infrared wavelengths in the past two decades (see, e.g., Raga et al. 2013 and Hodapp & Chini 2014, and references therein). These studies suggest that the proper motions of the jet range from $\sim 15 \text{ km s}^{-1}$ (inner jet; Hodapp & Chini 2014) to $\sim 40 \text{ km s}^{-1}$ (outer large-scale jet; e.g., Khanzadyan et al. 2003). Therefore, there is a possibility that the varying proper motions of the jet cause the unequal spacings between the bullets, which in turn results in the difference between the model and observations.

Since jets are accretion-driven, jet properties that change with time and space can provide important constraints on past temporal variations in the ejection/accretion system (see Arce et al. 2007; Frank et al. 2014). As seen in the SMA CO images, the bullets in the SVS 13 A jet, representing abrupt enhancements in velocity and density, are very likely the results of episodic ejections, as seen in other jets/outflows, e.g., HH 80-81 (Qiu & Zhang 2009), L1448C (Hirano et al. 2010), and HH 46/47 (Arce et al. 2013). As introduced in Section I, SVS 13 A itself also displays a high variability, similar to a FUor-type object (Hodapp & Chini 2014). Therefore, it is of interest to relate the episodic ejections of the bullets with the FUor-like outbursts of SVS 13 A. Based on the spacings between the blue bullets, the estimated period for the episodic ejections in the SVS 13 A jet is $\sim 240\text{--}830$ yr (depending on the proper motion velocities), which is consistent with the periods predicted for the FUor type outbursts (Audard et al. 2014).

4.2. Rotation of Bullets

SMA CO (2–1) observations show clear systematic velocity gradients, perpendicular to the jet axis, in both the blue bullet 2 and red bullet in the SVS 13 A jet. The velocity gradients

in the two bullets are roughly in the same direction. Although an obvious explanation is that the velocity gradients result from the rotation of the bullets, as introduced in Section I, several alternative interpretations for such systematic velocity gradients should also be considered, such as twin-jets configuration, jet precession, warped disk, and helical MHD shocks.

Based on an SMA dust continuum survey toward 33 Class 0 protostars, Chen et al. (2013) found that about two-thirds of protostars are binary/multiple systems, with separations ranging from 5000 down to 50 au. A higher angular resolution VLA survey further confirms a high multiplicity frequency in protostars with smaller separations ranging from 100 down to 10 au (Tobin et al. 2016). Therefore, it is necessary to consider the (non-rotating and non spatially resolved) twin-jets model that could possibly lead to the observed velocity field (see discussion in Launhardt et al. 2009). Indeed, Launhardt et al. (2009) and Soker & McIey (2013) found that the twin-jets scenario seems to apply to the cases of CB 26 and NGC 1333 IRAS 4A, respectively. In SVS 13 A, VLA radio observations detected a close binary system (VLA 4A and VLA 4B) with a separation of $\sim 0''.3$ (Anglada et al. 2000). However, higher angular resolution near-infrared observations ($\sim 0''.01$ or ~ 2.4 au) at the Keck telescopes clearly show that the high-velocity SVS 13 jet is driven only by source VLA 4B and no jet is detected from source VLA 4A (Hodapp & Chini 2014). The Keck results are consistent with the VLA observations that only source VLA 4B is associated with a circumstellar disk (and thus jet) in this binary system (Anglada et al. 2004). Therefore, both the Keck and VLA observations rule out the twin-jets configuration in the case of SVS 13 A.

Another potential explanation is that the SVS 13 A jet is a precessing (non-rotating) jet. The precession of the jet is driven by tidal interactions between the disk from which the jet is launched and a companion star on a non-coplanar orbit. In this scenario, the velocity gradient perpendicular to the jet axis is a result of outflow gas being entrained along different directions at different times. However, precessing jets generally produce point-symmetric (S-shaped) wiggles (see, e.g., L1157, Takami et al. 2011). If the velocity gradients in blue bullet 2 and the red bullet were indeed caused by a precessing jet, the directions of the velocity gradients in the two bullets would be in the opposite direction, but in the observations the velocity gradients of the two bullets are approximately in the same direction. Therefore, we consider that the precessing jet explanation does not apply to the case of SVS 13 A. Moreover, we note that it is still uncertain whether precession is able to produce velocity gradients mimicking rotation signatures in a jet. For example, three-dimensional molecular line simulations in Smith & Rosen (2007) found no signature for rotation in precessing jets, which is in contrast to the results of Cerqueira et al. (2006), who found velocity gradients in both rotating and precessing jets.

Suggested by Soker (2005), the interaction of a jet with a twisted-tilted (warped) disk may also produce observed asymmetry velocity profiles. In this scenario, there is an assumed inclination between the jet and the outer parts of the disk. Namely, the inner disk is perpendicular to the jet, while the outer disk flares in a point-symmetric manner: one side up and the opposite (relative to the central driving source) down. Another assumption in this scenario is that the jet interacts with the ambient gas above the disk surface and is more slowed down on the warped side of the disk than on the opposite side. Nevertheless, high angular resolution VLA observations show no hints for the existence of such warped outer disk around SVS 13 A (see Anglada et al. 2000, 2004; the disk radius around SVS 13 A is estimated to be ~ 32 au). Furthermore, in the calculations in Soker (2005), disk kinematics was apparently not taken into account. Since a warped disk should be rotating, it cannot simply slow down one side exclusively all the time. From the SMA CO observations, the (projected) length of blue bullet 2 is ~ 2600 au, and the estimated propagation time of bullet 2 is ~ 310 – 830 yr. Assuming that the SVS 13 A jet really interacts with the ambient gas above a warped disk at a radius of 10 au, the period of such interaction would be ~ 30 – 40 yr (considering a Keplerian disk around a source with a mass of ~ 0.8 – $1.0 M_{\odot}$). Therefore, during the propagation of blue bullet 2, the warped disk will interact roughly 10–30 times with each side of the jet. After so many times symmetrically interacting, the effect from the warped disk would be smoothed, and no asymmetry velocity profile would be expected in blue bullet 2.

Fendt (2011) suggested that helical MHD shocks can self-generate rotational motions. In this scenario, shock compression of a helical magnetic field results in a toroidal Lorentz force component that will accelerate the jet material in the toroidal direction. This process transforms magnetic angular momentum carried along the jet into kinetic angular momentum (rotation), although the jet is injected into the ambient gas with no initial rotation (see Fendt 2011 for details). Therefore, the motion caused by helical MHD shocks is real rotation and not a gradient that mimics rotation as the other alternative scenarios (i.e., twin-jets, precession, and warped disk). Nevertheless, helical MHD shocks only drive slow rotation, with a rotation speed of about 0.1%–1% of the jet bulk velocity (see Fendt 2011). The rotation velocity measured in blue bullet 2 is roughly 8 – 10 km s^{-1} , which is about 10% of the jet bulk velocity ($\sim 100 \text{ km s}^{-1}$) — significantly larger than that expected for rotation driven by helical MHD shocks. Hence, the probability of helical MHD shocks resulting in high velocity rotation of the bullets in SVS 13 A is extremely low.

After discussing the above alternative scenarios, the rotation of the bullets appears to be the preferred explanation left for the observed velocity fields in blue bullet 2 and the red bullet. However, a few uncertainties still need to be considered regarding this rotation explanation. The first question is why no rotation signature is seen in blue bullets 1 and 3

in the SMA CO observations. As introduced and discussed above, SVS 13 A is a FUor-like variable protostar with episodic outbursts. During outburst processes, high accretion rates lead to the onslaught of a large amount of material and angular momentum, which would then drive strong jets/outflows (due to the physical link between accretion and ejection), e.g., the bullets seen in the SVS 13 A jet. Nevertheless, theoretical studies also find large differences between episodic outbursts, with luminosity and accretion rate varying within at least one order of magnitude (see, e.g., Vorobyov & Basu 2010; 2015). This is consistent with the results from numerical simulations of protostellar outflows, in which the properties of young outflows (e.g., mass, luminosity, and momentum) vary with stellar evolution, due to episodic accretion (see, e.g., Machida & Hosokawa 2013; Machida 2014). Hence, there is a possibility that blue bullet 2 and the red bullet result from bursts with somehow more angular momentum loss (or clearer transverse velocity gradients), while blue bullets 1 and 3 result from relatively weaker bursts, whose underlying rotation signature is not easily distinguished in the observations (see below).

As reviewed by Ray et al. (2007) and Belloche (2013), the detection of the rotation of jets/outflows is extremely difficult, not only because both high angular and spectral resolution are required, but also the kinematics of jets/outflows is complicated (including acceleration, rotation, and interaction with the environment, etc.). As shown in the velocity channel maps (see Fig. 8), the transverse velocity gradient is not seen in the velocity range between -128 and -112 km s^{-1} for blue bullet 2 (a high-velocity front of blue bullet 2 in morphology), but much clearer in the velocity range between -110 and -85 km s^{-1} (which is shown in Figure 2). Including both velocity ranges, the velocity field is more complicated and the so-called ‘Hubble-law’ effect appears in the field. A similar situation seems to happen in blue bullet 1 (see velocity channel maps shown in Figure 8). Although no clear transverse velocity gradient is detected in its high velocity emission (from -114 to -70 km s^{-1} ; dominated by the ‘Hubble-law’ effect, see Figure 2), a velocity shift, away from the driving source but perpendicular to the local jet, is tentatively detected in the velocity between -70 and -40 km s^{-1} . Figure 5 shows the velocity fields of blue bullet 1 in this velocity range. The direction of this tentative velocity gradient is consistent with that of blue bullet 2 shown in Fig. 2, i.e., the left side of the local jet axis is blueshifted while the right side is redshifted. So, there is a possibility that blue bullet 1 is also rotating, but its rotation signature (i.e., transverse velocity gradient) is more hidden or confused by its complicated kinematics (compared with blue bullet 2), which can only be indistinctly seen in a certain velocity range. We also note that the comparison between the SMA CO observations (this work) and the Keck [Fe II] observations (Hodapp & Chini 2014) shows a tentative velocity gradient across the microjet detected in the Keck images, which is consistent with that found in blue bullet 2 in the SMA CO images (see Appendix B).

Another uncertainty of the rotation explanation comes from the driving disk of the jet. To our knowledge, the kinematics of the circumstellar disk around SVS 13 A is unknown yet. As suggested by Belloche (2013), one important requirement for convincingly detecting rotation in jets is that the velocity gradients should be consistent between both outflow lobes and with the disk rotation. Due to insufficient observations, this requirement is still missing in the SVS 13 A jet system.

In summary, due to the uncertainties discussed above, the detection of the rotation of the bullets in the SVS 13 A jet is *not* definitive yet. Based on the SMA CO (2–1) observations, we consider the rotation of the bullets thus far the most likely explanation for the observed velocity fields in blue bullet 2 and the red bullet. Hereafter we analyze the properties of the two bullets according to this explanation. It must be noted that further high angular resolution observations are needed to comprehensively study the kinematics of the SVS 13 A jet, as well as the disk of the driving source, in order to confirm the rotation nature of these bullets.

4.3. Angular Momenta in the Bullets

For the EHV bullets in the SVS 13 A jet (velocities $> 70 \text{ km s}^{-1}$ and no ^{13}CO line emission detected at these velocity ranges), the CO (2–1) emission can be safely regarded as optically thin. The gas masses of the bullets are then derived with the same method as described in Cabrit & Bertout (1990). In the calculations, we assume LTE conditions, and excitation temperatures of 25 K and 45 K for the blue and red bullets, respectively, which were derived from single-dish CO (2–1)/(1–0) observations (see Masson et al. 1990). The estimated bullet masses are then $\sim 3.8 \times 10^{-4}$ and $\sim 3.1 \times 10^{-4} M_{\odot}$ for blue bullet 2 and the red bullet, respectively. The masses of the other bullets, as well as other jet properties, will be presented and discussed in future work.

Based on the SMA CO PV diagrams (see Figure 3), rotation velocity v_{ϕ} and radius R_{rot} of the two bullets are measured between the blue and red peaks in the PV diagrams, corrected for the inclination angle ($i = 40^{\circ}$), i.e.,

$$v_{\phi} = \frac{1}{\sin i} \frac{v_{\text{shift}}}{2}, \quad (2)$$

$$R_{\text{rot}} = \frac{L_{\text{shift}}}{2}. \quad (3)$$

The measured rotation velocities and radii are $\sim 11.7\text{--}13.7 \text{ km s}^{-1}$ and $\sim 440\text{--}610 \text{ au}$ for blue bullet 2, and $\sim 4.7 \pm 0.5 \text{ km s}^{-1}$ and $\sim 1200 \pm 200 \text{ au}$ for the red bullet. These rotation velocities are comparable to the values measured in the rotating jet in DG Tau ($6\text{--}15 \text{ km s}^{-1}$;

Bacciotti et al. 2002), but much larger than those measured in other rotating outflow candidates, e.g., CB 26 ($1\text{--}2\text{ km s}^{-1}$; Launhardt et al. 2009). The estimated local specific angular momentum ($v_\phi \times R_{\text{rot}}$) for the two rotating bullets is $j_{\text{blue bullet}} \sim 9.8 \times 10^{21} \text{ cm}^2 \text{ s}^{-1}$ and $j_{\text{red bullet}} \sim 8.5 \times 10^{21} \text{ cm}^2 \text{ s}^{-1}$, respectively. The specific angular momenta of the two bullets are much higher than that of the rotating jet in DG Tau ($\sim 3.5 \times 10^{20} \text{ cm}^2 \text{ s}^{-1}$; Bacciotti et al. 2002) and that of the rotating outflow in CB 26 ($\sim 1.5 \times 10^{20} \text{ cm}^2 \text{ s}^{-1}$; Launhardt et al. 2009). It may imply that rotating jets from episodic outbursts in the protostellar phase can more efficiently remove the (specific) angular momentum from the star-disk system, compared with outflows in the T Tauri phase.

For a further comparison, we present the two rotating bullets in Figure 6, which shows the distribution of specific angular momentum as a function of rotation radius for different scales of a star forming region – from molecular clouds, through protostellar envelopes, circumstellar disks, and binaries, all the way to the Sun. This figure is mainly based on the diagram published by Belloche (2013, and references therein). As seen in Figure 6, the specific angular momenta of the two rotating bullets are comparable to those of dense cores, about 10 times larger than those of protostellar envelopes, and about 20 times larger than those of circumstellar disks (also corrected for inclination; see Belloche 2013). The large amount of specific angular momenta associated with the two bullets indicates that the rotation of the jets/outflows may be the most efficient method in extracting angular momentum in the early phases of star formation. It should be noted that the total angular momenta (mass being taken into account) of these circumstellar disks are still larger than those of the bullets, considering that the disk mass of embedded protostars (disk masses ranging from ~ 0.02 to $\sim 0.1 M_\odot$ with a median of $0.04 M_\odot$; see a review by Williams & Cieza 2011) is hundreds of times larger than the masses of the bullets. Note that, for the SVS 13 A jet, the disk mass of the driving source was estimated to be $\sim 0.06 M_\odot$ (Anglada et al. 2004).

The comparison suggests that most of the angular momentum of a protostellar circumstellar disk can be extracted by only a few tens of such rotating bullets produced by episodic outbursts. Interestingly, based on the IRAS survey, Kenyon et al. (1990) estimated that each YSO experiences at least 10 FUor-type outbursts during its evolution. Recent theoretical simulations also suggest that YSOs will experience roughly 20–30 outbursts during the early phase of star formation (see, e.g., Vorobyov & Basu 2015). The tentative discovery of rotating bullets in the SVS 13 A jet, as well as their large angular momentum, would be consistent with this episodic accretion/burst scenario in star formation.

4.4. Launching Mechanism of Bullets

The precise origin of jets from YSOs is still hotly debated. Theoretical studies have suggested several launching models for jets, including stellar wind, X-wind, and disk-wind (see Pudritz et al. 2007; Shang et al. 2007; Frank et al. 2014). The jet launching radii, depending on the launching models, range from a few R_\odot (stellar wind), ≤ 0.1 au (X-wind), to possibly several au (disk-wind). As reviewed by Ray et al. (2007) and Frank et al. (2014), a key observational diagnostic to discriminate between these models is to search for signatures of rotation in jets/outflows, and then to infer the launching ‘footprint’. Thus far most studies, which interpret the observed velocity gradients perpendicular to the outflow axis as due to jet rotation, seem to be consistent with an origin from an extended disk-wind, launched from between 0.1 to 3–5 au (see Cabrit 2009; Frank et al. 2014). However, it must be noted that these observations cannot exclude the existence of inner stellar or X-winds because only external structures of the jet have been observed due to limited angular resolution.

We also estimate the launching footprint of the SVS 13 A jet based on the presumed rotational signature of blue bullet 2 (which has a more systematic velocity field and higher signal-to-noise ratio, as compared with the red bullet), using the equation suggested by Anderson et al. (2003):

$$R_0 \approx 0.7 \text{ au} \left(\frac{R}{10 \text{ au}} \right)^{2/3} \left(\frac{v_{\phi,R}}{10 \text{ km s}^{-1}} \right)^{2/3} \left(\frac{v_{p,R}}{100 \text{ km s}^{-1}} \right)^{-4/3} \left(\frac{M_\star}{1 M_\odot} \right)^{1/3}. \quad (4)$$

In the equation, $v_{\phi,R}$ and $v_{p,R}$ are toroidal and poloidal velocities at a distance R from the jet axis, respectively. Based on the SMA CO PV diagrams (see Figure 3), toroidal and poloidal velocities are measured using the following equations,

$$v_{\phi,R} = \frac{1}{\sin i} \frac{v_{\text{blue peak}} - v_{\text{red peak}}}{2}, \quad (5)$$

$$v_{p,R} = \frac{1}{\cos i} \frac{v_{\text{blue peak}} + v_{\text{red peak}}}{2}. \quad (6)$$

In the calculations, the mass of the driving source M_\star is adopted as $\sim 1.0 M_\odot$ (see Chen et al. 2009) and inclination angle i as 40° . The estimated launching footprint for blue bullet 2 is then $\sim 7.2\text{--}7.7$ au, which appears to support the extended disk-wind model. Note that the disk radius of SVS 13 A was estimated to ~ 32 au (Anglada et al. 2004), which is about 4–5 times larger than the launching radius for blue bullet 2.

5. SUMMARY

We present SMA CO (2–1) observations toward the well-known prototellar jet driven by SVS 13 A, a variable protostar in the NGC 1333 star-forming region. SMA CO images show high-velocity jets from SVS 13 A, with velocities ranging from ~ -150 to ~ 150 km s $^{-1}$. In this work, we focus on the extremely high velocity (EHV) components (jet velocities > 70 km s $^{-1}$ over the cloud systemic velocity), the so-called molecular bullets. The main results of this work are summarized below.

(1) Three bullets are found in the blueshifted jet (blue bullets), and one bullet is found in the redshifted jet (red bullet). The blueshifted jet shows a wiggle morphology, which can be reasonably fitted by an orbiting-jet model. The best-fit parameters suggest that the source itself is a binary system with an orbital radius of $0''.16 \pm 0''.02$, which is consistent with previous VLA observations. Considering that SVS 13 A is a FUor-like variable protostar, we suggest that the bullets in the SVS 13 jet are formed by periodic bursts of mass, which take place every few hundred years.

(2) Based on the SMA CO (2–1) observations, we discover in one blueshifted bullet (blue bullet 2) and the redshifted bullet clear and large systematic velocity gradients, perpendicular to the jet axis. The velocity gradients in the blue- and redshifted bullets are roughly in the same direction. After discussing several scenarios, such as twin-jets, jet precession, warped disk, and helical shock, we suggest that the observed velocity gradients in the bullets most likely result from the rotation of the SVS 13 A jet.

(3) From the SMA CO images, the measured rotation velocities are ~ 11.7 – 13.7 km s $^{-1}$ for the blueshifted bullet and $\sim 4.7 \pm 0.5$ km s $^{-1}$ for the redshifted bullet. The estimated specific angular momenta are $\sim 9.8 \times 10^{21}$ cm 2 s $^{-1}$ for the blueshifted bullet and $\sim 8.5 \times 10^{21}$ cm 2 s $^{-1}$ for the redshifted bullet, which are comparable with those of dense cores, about 10 times larger than those of protostellar envelopes and about 20 times larger than those of circumstellar disks. The significant amount of specific angular momenta associated with the two bullets indicates that the rotation of the jets/outflows is an efficient method in extracting angular momentum in the early phases of star formation, which may be a key mechanism to resolve the “angular momentum problem” in the field of star formation.

(4) Based on the jet kinematics derived from SMA CO observations, the estimated launching footprint on the disk has a radius of ~ 7.2 – 7.7 au, which appears to support the extended disk-wind model.

(5) Nevertheless, due to remaining uncertainties (e.g., absence of clear signs of rotation in the other bullets), the detection of the jet rotation in SVS 13 A is not definitive yet. Further observations are needed to comprehensively understand the kinematics of the SVS 13 A jet

system (including circumstellar disk), in order to confirm the rotation nature of the bullets.

We thank the anonymous referee for providing many insightful suggestions and comments, which helped us to improve this work. We acknowledge the SMA staff for technical support during the observations. We thank K. W. Hodapp for providing us Keck [FeII] data. This work was supported by the National Natural Science Foundation of China (grants Nos. 11473069 and 11328301) and the Strategic Priority Research Program of the Chinese Academy of Sciences (grant No. XDB09000000). X.C. acknowledges the support of the Thousand Young Talents Program of China.

A. SMA CO (2–1) Velocity Channel Maps of Bullets

In this Appendix, we present the SMA CO (2–1) velocity channel maps of blue bullet 3 (Figure 7), blue bullets 2 & 1 (Figure 8), and the red bullet (Figure 9). For all these channel maps, the phase center is R.A. = $03^{\text{h}}29^{\text{m}}03^{\text{s}}.07$, decl. = $31^{\circ}15'52''.00$ (J2000). The center velocity of the channel is written in the top left corner of each panel (in km s^{-1}), while the filled grey ellipse (lower right corner) in each panel indicates the SMA synthesized beam. The systemic velocity of the cloud is $\sim 9 \text{ km s}^{-1}$.

B. The Comparison Between SMA CO and Keck [Fe II] Data

In this Appendix, we compare the SMA CO (2–1) observations with the Keck [Fe II] $1.644 \mu\text{m}$ near-infrared observations. The inner microjet in SVS 13 A was observed in the [Fe II] line at the Keck telescopes in 2012 and 2013 (Hodapp & Chini 2014). Interestingly, the 2012 Keck image shows a tentative detection of a velocity gradient across the driving source (see Figure 10). This velocity gradient is perpendicular to the microjet and is in the same direction as those in blue bullet 2 and red bullet seen in the SMA CO (2–1) observations. In this context, the velocity gradient seen in the 2012 Keck image could be interpreted as the rotation of the microjet, in comparison with the SMA CO velocity fields of the bullets. However, it must be noted that the velocity gradient seen in the 2012 Keck image is not seen in the 2013 Keck image. Figure 11 shows a comparison between the 2012 and 2013 Keck data. As seen in Fig. 11, the 2013 data around the driving source do not extend as much as the 2012 data (top panels); furthermore, the noise level around the driving source is about $10\text{--}20 \text{ km s}^{-1}$ in the 2012 image, but about 30 km s^{-1} in the 2013 image (bottom panels). The velocity shift across the driving source seen in the 2012 image is about $60\text{--}70 \text{ km s}^{-1}$, which is only ~ 2 times larger than the noise levels in the 2013 image. Therefore, the absence of the velocity gradient in the 2013 image is probably due to: (1) the region that appears to show a velocity gradient is not fully detected in the 2013 observations, and (2) relatively lower signal-to-noise ratios in this region.

We note that Hodapp & Chini (2014) tried to find rotation signature in the SVS 13 A microjet, but concluded they do not detect any rotation. Indeed, including both the 2012 and 2013 Keck data, it will be difficult to distinguish any velocity gradient, due to the difference between the two epoch data. Further high angular resolution observations at the Keck telescopes (or other large telescopes) are needed to confirm the detection of the velocity gradient across the driving source seen in the 2012 Keck data.

REFERENCES

- Anderson, J. M., Li, Z.-Y., Krasnopolsky, R., & Blandford, R. D. 2003, *ApJ*, 590, L107
- Anglada, G., López, R., Estalella, R., et al. 2007, *AJ*, 133, 2799
- Anglada, G., Rodríguez, L. F., Osorio, M., et al. 2004, *ApJ*, 605, L137
- Anglada, G., Rodríguez, L. F., & Torrelles, J. M. 2000, *ApJ*, 542, L123
- Arce, H. G., & Goodman, A. A. 2001, *ApJ*, 551, L171
- Arce, H. G., Mardones, D., Corder, S. A., et al. 2013, *ApJ*, 774, 39
- Arce, H. G., Shepherd, D., & Gueth, F., et al. 2007, in *Protostars and Planets V*, ed. B. Reipurth, D. Jewitt, & K. Keil (Tucson: Univ. Arizona Press), 245
- Audard, M., Ábrahám, P., Dunham, M. M., et al. 2014, in *Protostars and Planets VI*, ed. H. Beuther, R. S. Klessen, C. P. Dullemond, & Th. Henning (Tucson: Univ. Arizona Press), 387
- Bacciotti, F. 2009, *Protostellar Jets in Context*, ed. K. Tsinganos, T. Ray, & M. Stute (Berlin: Springer), 231
- Bacciotti, F., Ray, T. P., Mundt, R., Eisloffel, J., & Solf, J. 2002, *ApJ*, 576, 222
- Bachiller, R., & Cernicharo, J. 1990, *A&A*, 239, 276
- Bachiller, R., Gueth, F., Guilloteau, S., Tafalla, M., & Dutrey, A. 2000, *A&A*, 362, L33
- Bachiller, R., Guilloteau, S., Gueth, F., et al. 1998, *A&A*, 339, L49
- Belloche, A. 2013, in *Angular Momentum Transport During the Formation and Early Evolution of Stars*, ed. P. Hennebelle & C. Charbonnel, *EAS Publications Series*, 62, 25
- Belloche, A., André, P., Despois, D., & Blinder, S. 2002, *A&A*, 393, 927
- Blandford, R. D., & Payne, D. G. 1982, *MNRAS*, 199, 883
- Bodenheimer, P. 1995, *ARA&A*, 33, 199
- Cabrit, S. 2009, *Protostellar Jets in Context*, ed. K. Tsinganos, T. Ray, & M. Stute (Berlin: Springer), 247

- Cabrit, S., & Bertout, C. 1990, *ApJ*, 348, 530
- Cerqueira, A. H., Velázquez, P. F., Raga, A. C., Vasconcelos, M. J., & de Colle, F. 2006, *A&A*, 448, 231
- Chen, X., Arce, H. G., Zhang, Q., et al. 2013, *ApJ*, 768, 110
- Chen, X., Launhardt, R., & Henning, Th. 2007, *ApJ*, 669, 1058
- Chen, X., Launhardt, R., & Henning, Th. 2009, *ApJ*, 691, 1729
- Choi, M., Kang, M., & Tatematsu, K. 2011, *ApJ*, 728, L34
- Codella, C., Cabrit, S., Gueth, F., et al. 2007, *A&A*, 462, L53
- Coffey, D., Bacciotti, F., Ray, T. P., Eisloffel, J., & Woitas, J. 2007, *ApJ*, 663, 350
- Correia, S., Zinnecker, H., Ridgway, S. T., & McCaughrean, M. J. 2009, *A&A*, 505, 673
- Davis, C. J., Ray, T. P., Desroches, L., & Aspin, C. 2001, *MNRAS*, 326, 524
- Fendt, C. 2011, *ApJ*, 737, 43
- Fendt, C., & Zinnecker, H. 1998, *A&A*, 334, 750
- Frank, A., Ray, T. P., Cabrit, S., et al. 2014, in *Protostars and Planets VI*, ed. H. Beuther, R. S. Klessen, C. P. Dullemond, & Th. Henning (Tucson: Univ. Arizona Press), 451
- Hartmann, L. 2009, *Protostellar Jets in Context*, ed. K. Tsinganos, T. Ray, & M. Stute (Berlin: Springer), 23
- Hartmann, L., & Kenyon, S. J. 1996, *ARA&A*, 34, 207
- Hirano, N., Ho, P. P. T., Liu, S.-Y., et al. 2010, *ApJ*, 717, 58
- Hirota, T., Bushimata, T., Choi, Y. K., et al. 2008, *PASJ*, 60, 37
- Ho, P. T. P., Moran, J. M., & Lo, K. Y. 2004, *ApJ*, 616, L1
- Hodapp, K. W., & Chini, R. 2014, *ApJ*, 794, 169
- Khanzadyan, T., Smith, M. D., Davis, C. J., et al. 2003, *MNRAS*, 338, 57
- Kenyon, S. J., Hartmann, L. W., Strom, K. M., & Strom, S. E. 1990, *AJ*, 99, 869
- Lada, C. J., & Fich, M. 1996, *ApJ*, 459, 638

- Launhardt, R., Pavlyuchenkov, Y., Gueth, F., et al. 2009, *A&A*, 494, 147
- Lee, C.-F., Hasegawa, T. I., Hirano, N., Palau, A., & Shang, H., et al. 2010, *ApJ*, 713, 731
- Lee, C.-F., Hirano, N., Palau, A., Ho, P. T. P., & Bourke, T. L. 2009, *ApJ*, 699, 1584
- Lee, C.-F., Ho, P. T. P., Bourke, T. L., Hirano, N., Shang, H., & Zhang, Q. 2008, *ApJ*, 685, 1026
- Lee, C.-F., Ho, P. T. P., Palau, A., Hirano, N., & Bourke, T. L., et al. 2007, *ApJ*, 670, 1188
- Machida, M. N. 2014, *ApJ*, 796, L17
- Machida, M. N., & Hosokawa, T. 2013, *MNRAS*, 431, 1719
- Masciadri, E., & Raga, A. C. 2002, *ApJ*, 568, 733
- Masson, C. R., Mundy, L. G., & Keene, J. 1990, *ApJ*, 357, L25
- Pech, G., Zapata, L. A., Loinard, L., & Rodríguez, L. F. 2012, *ApJ*, 751, 78
- Pesenti, N., Dougados, C., Cabrit, S., et al. 2004, *A&A*, 416, L9
- Plunkett, A. L., Arce, H. G., Corder, S. A., et al. 2013, *ApJ*, 774, 22
- Pudritz, R. E., Ouyed, R., Fendt, C., & Brandenburg, A. 2007, *Protostars and Planets V*, ed. B. Reipurth, D. Jewitt, & K. Keil (Tucson: Univ. Arizona Press), 277
- Qi, C. 2005, *MIR Cookbook* (Cambridge: Harvard), <http://cfa-www.harvard.edu/cqi/mircook.html>
- Qiu, K., & Zhang, Q. 2009, *ApJ*, 702, L66
- Raga, A. C., Noriega-Crespo, A., Carey, S. J., & Arce, H. G. 2013, *AJ*, 145, 28
- Ray, T., Dougados, C., Bacciotti, F., Eisloffel, J., & Chrysostomou, A. 2007, *Protostars and Planets V*, ed. B. Reipurth, D. Jewitt, & K. Keil (Tucson: Univ. Arizona Press), 231
- Reipurth, B., & Bally, J. 2001, *ARA&A*, 39, 403
- Rodríguez, L. F., Zapata, L. A., & Palau, A. 2014, *ApJ*, 790, 80
- Safron, E. J., Fischer, W. J., Megeath, S. T., et al. 2015, *ApJ*, 800, L5

- Sault, R. J., Teuben, P. J., & Wright, M. C. H. 1995, in ASP Conf. Ser. 77, *Astronomical Data Analysis Software and Systems IV*, ed. R. A. Shaw, H. E. Payne, & J. J. E. Hayes (San Francisco, CA: ASP), 443
- Shang, H., Li, Z.-Y., & Hirano, N. 2007, *Protostars and Planets V*, ed. B. Reipurth, D. Jewitt, & K. Keil (Tucson: Univ. Arizona Press), 261
- Smith, M. D., & Rosen, A. 2007, *MNRAS*, 378, 691
- Soker, N. 2005, *A&A*, 435, 125
- Soker, N., & Mcley, L. 2013, *ApJ*, 772, L22
- Spitzer, L. 1978, *Physical processes in the interstellar medium*, New York Wiley-Interscience
- Strom, S. E., Vrba, F. J., & Strom, K. M. 1976, *AJ*, 81, 314
- Takami, M., Chrysostomou, A., Ray, T. P., et al. 2006, *ApJ*, 641, 357
- Takami, M., Karr, J. L., Nisini, B., & Ray, T. P. 2011, *ApJ*, 743, 193
- Tobin, J. J., Hartmann, L., Chiang, H.-F., et al. 2011, *ApJ*, 740, 45
- Tobin, J. J., Looney, L. W., Li, Z.-Y., et al. 2016, *ApJ*, 818, 73
- Vorobyov, E. I., & Basu, S. 2010, *ApJ*, 719, 1896
- Vorobyov, E. I., & Basu, S. 2015, *ApJ*, 805, 115
- Williams, J. P., & Cieza, L. A. 2011, *ARA&A*, 49, 67
- Zapata, L. A., Ho, P. T. P., Rodríguez, L. F., Schilke, P., & Kurtz, S. 2007, *A&A*, 471, L59
- Zapata, L. A., Schilke, P., & Ho, P. T. P. 2010a, *MNRAS*, 402, 2221
- Zapata, L. A., Schmid-Burgk, J., Muders, D., et al. 2010b, *A&A*, 510, A2

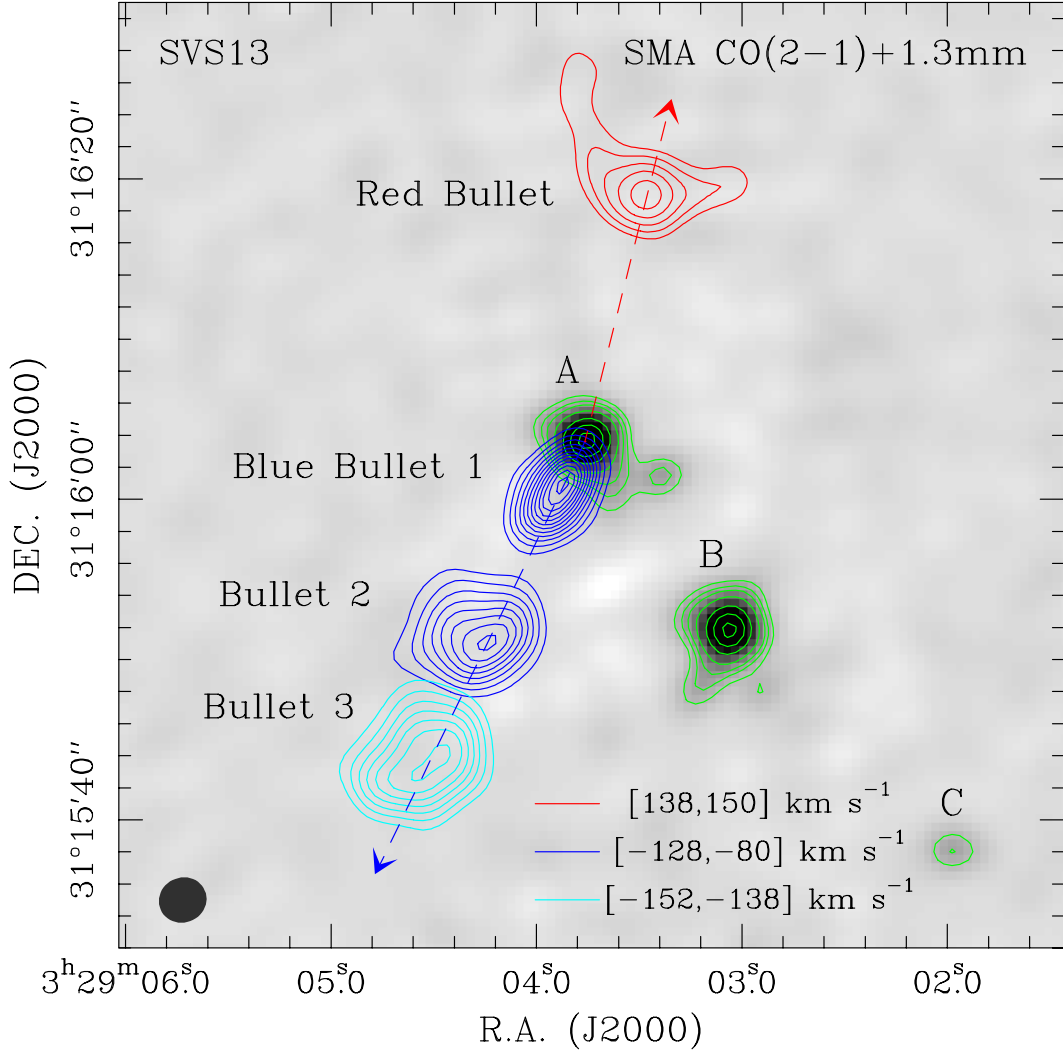


Fig. 1.— Velocity-integrated intensity maps of the SMA CO (2–1) emission from SVS 13, plotted on the SMA 1.3mm dust continuum image (grey image and green contours; from Chen et al. 2013). The red, blue, and cyan contours represent CO (2–1) emission integrated over three different velocity ranges shown in the image, which is redshifted or blueshifted with respect to the cloud systemic velocity ($\sim 9 \text{ km s}^{-1}$). The CO red contours start at $0.64 \text{ Jy beam}^{-1} \text{ km s}^{-1}$ ($\sim 4\sigma$) and increase in steps of $0.32 \text{ Jy beam}^{-1} \text{ km s}^{-1}$ ($\sim 2\sigma$), blue contours start at $1.6 \text{ Jy beam}^{-1} \text{ km s}^{-1}$ ($\sim 4\sigma$) and increase in steps of $1.2 \text{ Jy beam}^{-1} \text{ km s}^{-1}$ ($\sim 3\sigma$), while cyan contours start at $0.64 \text{ Jy beam}^{-1} \text{ km s}^{-1}$ ($\sim 4\sigma$) and increase in steps of $0.48 \text{ Jy beam}^{-1} \text{ km s}^{-1}$ ($\sim 3\sigma$). The three dust continuum sources found in the region are named A, B, and C, respectively (see Chen et al. 2013). The blue and red dashed line arrows show the overall directions of the blueshifted and redshifted jets from source SVS 13 A. The grey oval in the bottom left corner indicates the SMA synthesized beam.

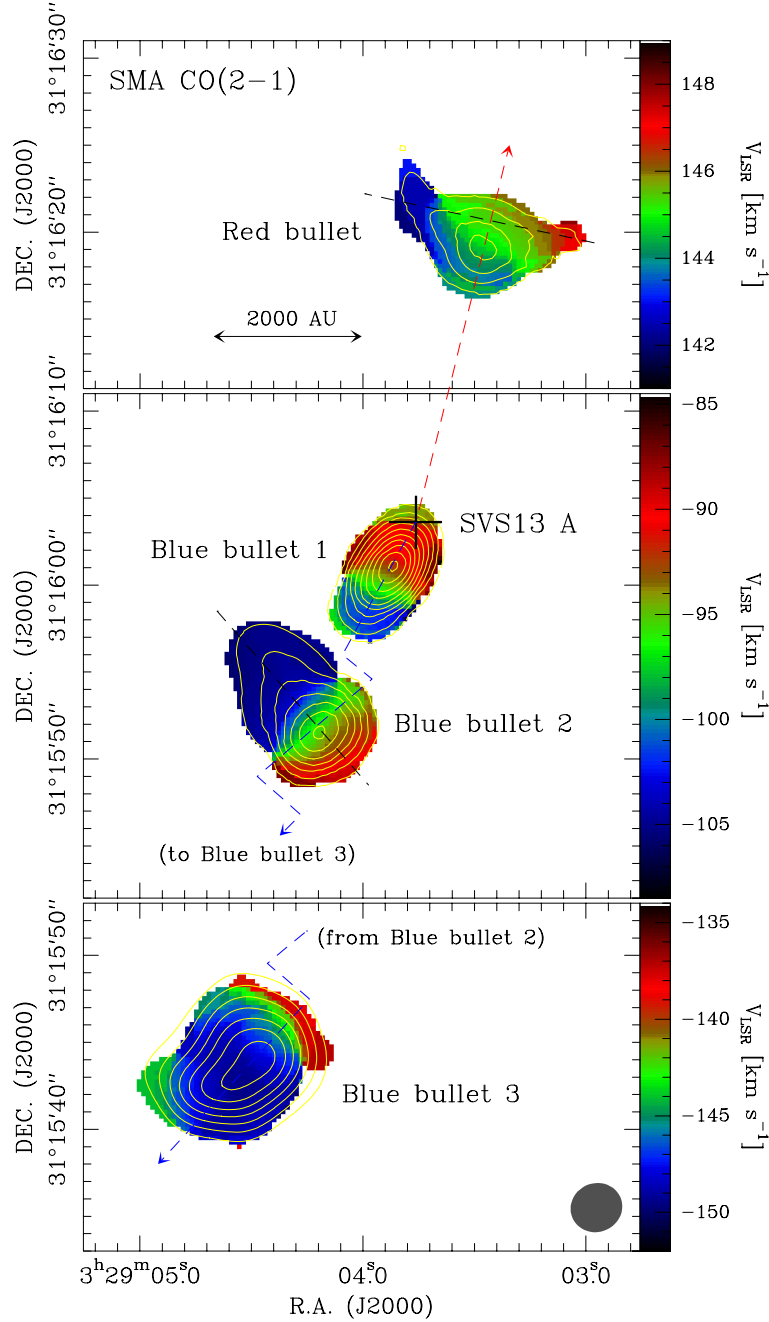


Fig. 2.— SMA CO(2–1) integrated intensity map (yellow contours) and mean velocity field (1st moment velocity map, color shades) of the SVS 13 A jet. *Top panel:* Red bullet (velocities integrated from +142 to +150 km s^{−1}). Contours start at 4σ and then increase in steps of 3σ (1σ ∼ 0.16 Jy beam^{−1} km s^{−1}). *Middle panel:* Blue bullets 1 and 2 (velocities integrated from −106 to −83 km s^{−1}). Contours start at 4σ and then increase in steps of 4σ (1σ ∼ 0.30 Jy beam^{−1} km s^{−1}). *Bottom panel:* Blue bullet 3 (velocities integrated from −154 to −134 km s^{−1}). Contours start at 3σ and then increase in steps of 3σ (1σ ∼ 0.18 Jy beam^{−1} km s^{−1}). The blue dashed line arrows shows the jet axis defined by the jet wiggle (see text). The cross marks the peak position of the dust continuum source, while the grey oval in the bottom right corner indicates the SMA synthesized beam.

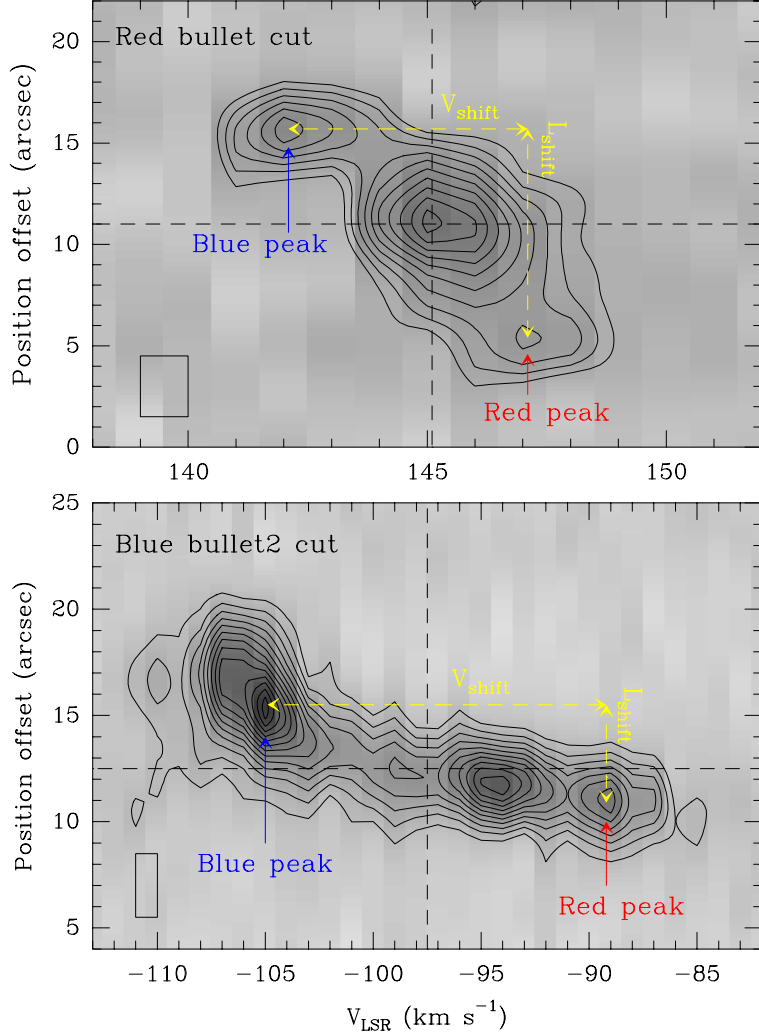


Fig. 3.— Position-velocity diagrams of the transversal cuts marked in Figure 2. *Top panel:* Cut across the red bullet. Contours start at 84 mJy beam^{-1} ($\sim 3\sigma$) and increase in steps of 28 mJy beam^{-1} ($\sim 1\sigma$). *Bottom panel:* Cut across the blue bullet 2. Contours start at $108 \text{ mJy beam}^{-1}$ ($\sim 3\sigma$) and increase in steps of 72 mJy beam^{-1} ($\sim 2\sigma$). The yellow dashed line arrows show the velocity shift (V_{shift}) and shift distance (L_{shift}) between the blue and red peaks. The rectangle in the bottom left of the two panels shows the velocity and angular resolutions of the observations. The two black dashed lines mark the position of the symmetry axis and radial mean velocity of the two bullets.

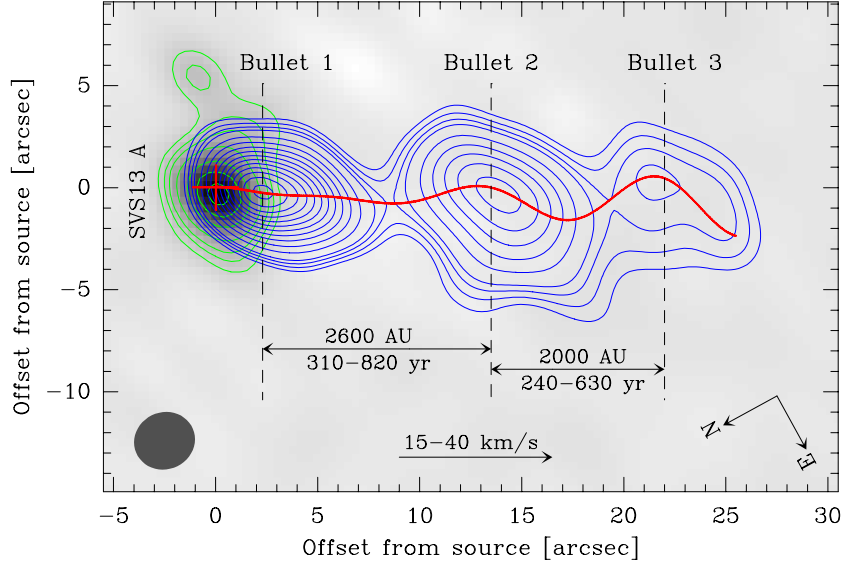


Fig. 4.— Velocity-integrated intensity map of the SMA CO (2–1) emission from SVS 13 A (blue contours), plotted on the SMA 1.3 mm dust continuum image (grey image and green contours). The maps have been rotated by 241.2 degree clockwise. The CO emission is integrated over the velocities ranging from -152 to -70 km s^{-1} , and contours correspond to 8, 12, 16, 20 σ and then increase in steps of 10 σ ($1 \sigma \sim 0.16 \text{ Jy beam}^{-1} \text{ km s}^{-1}$). The red cross marks the peak position of the SVS 13 A dust continuum source, while the red wavy curve shows the best-fit of the orbiting source jet model to the CO integrated emission. The black arrow in the bottom shows the proper motions of the jet (in a velocity range of $15\text{--}40$ km s^{-1} ; see text), while the periods shown in the map are estimated from the spacings between the bullets and the proper motions of the jet.

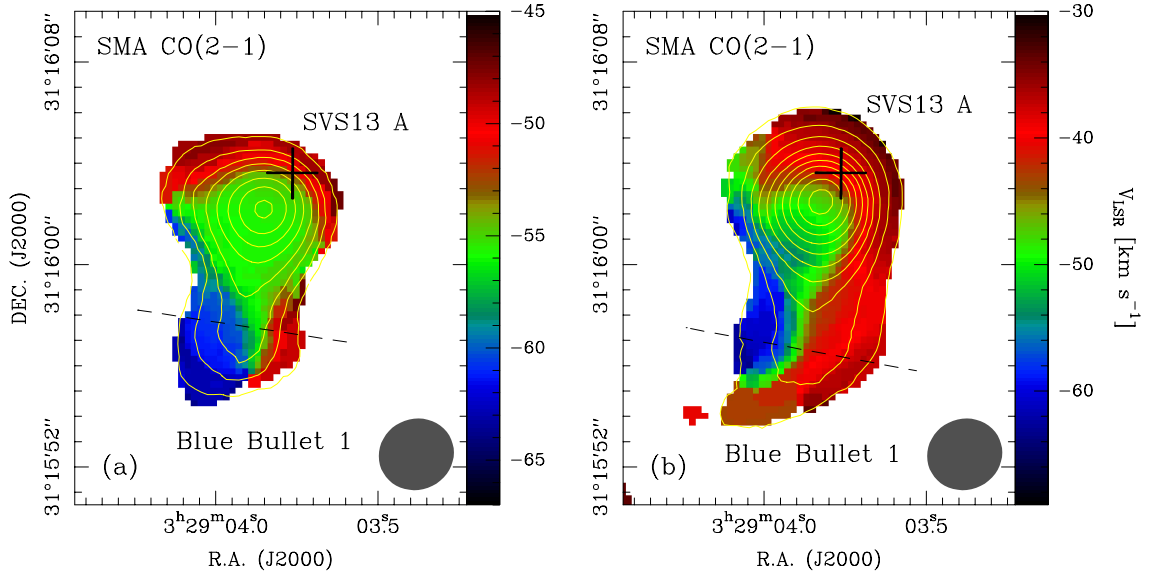


Fig. 5.— (a) SMA CO(2–1) velocity-integrated intensity map (yellow contours) and mean velocity field (1st moment velocity map, color shades) of the SVS13 A jet (velocities from -66 to -47 km s⁻¹). Contours start at 5σ and then increase in steps of 4σ ($1\sigma \sim 0.24$ Jy beam⁻¹ km s⁻¹). (b) Similar as panel a, but velocities integrated from -75 to -30 km s⁻¹. Contours start at 6σ and then increase in steps of 5σ ($1\sigma \sim 0.43$ Jy beam⁻¹ km s⁻¹). In the two panels, the cross marks the peak position of the dust continuum source SVS13 A, while the grey oval in the bottom right corner indicates the SMA synthesized beam. The dashed lines show the directions of the tentative velocity gradients seen across the low-velocity part of blue bullet 1.

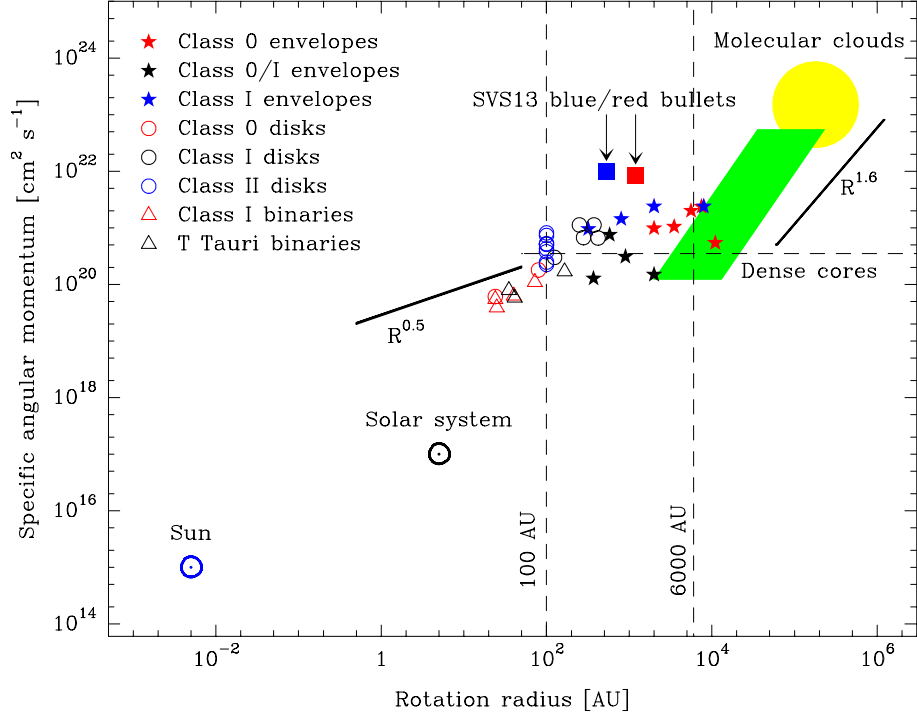


Fig. 6.— Specific angular momentum as a function of different scales of a star forming region. The specific angular momentum is the local value (i.e., the product of the rotation velocity and the radius) for all categories except for the binaries, the solar system, and the Sun for which it corresponds to the mean angular momentum per unit of mass (see Belloche 2013 and references therein). Yellow filled circle and green filled parallelogram show the approximate positions for the distributions of molecular clouds and dense cores, respectively. For all disks and most of protostellar envelopes, as well as the two rotating bullets from SVS 13 A (red and blue squares), the values have been corrected for inclination. The two solid lines are shown to guide the eye; they are not least-square fits to the data. The vertical dashed lines mark the approximate position of breaks in the distribution of angular momentum and the horizontal one indicates the typical specific angular momentum during the protostellar collapse phase (see Belloche 2013 for more details).

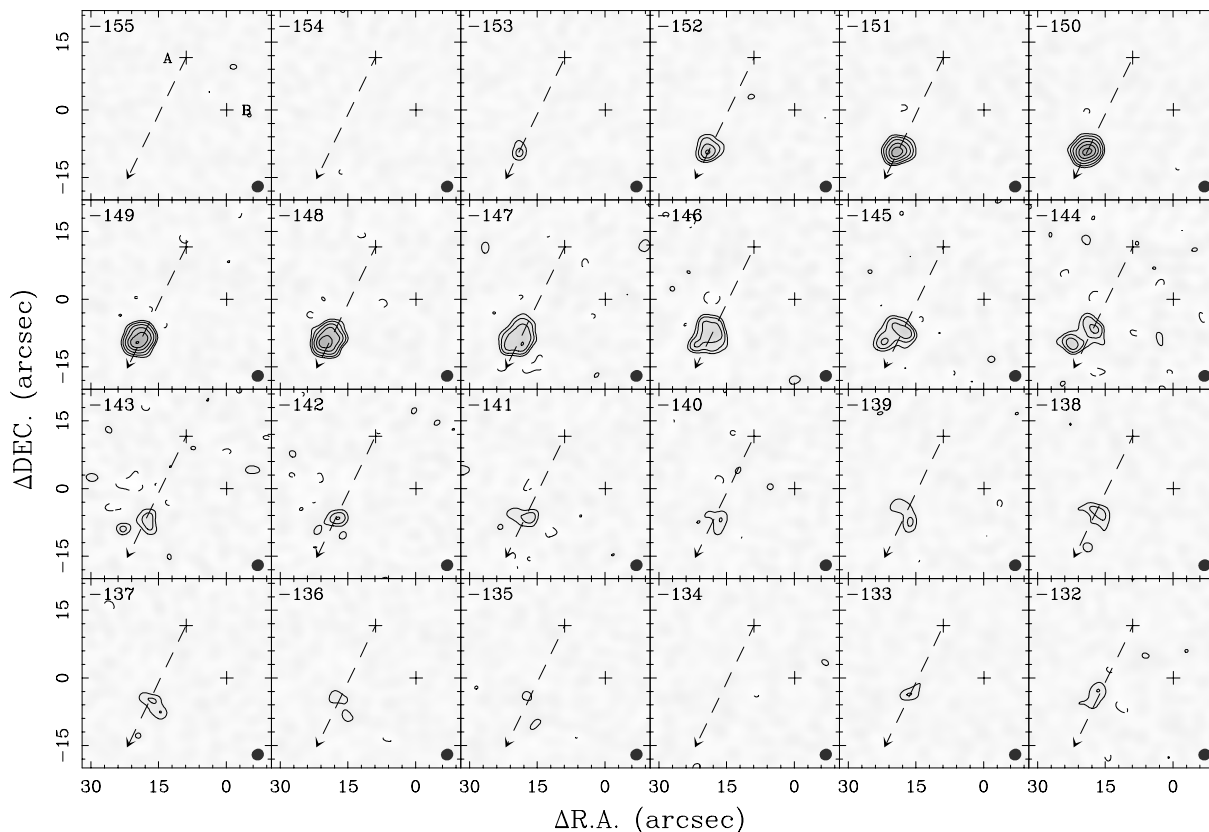


Fig. 7.— SMA CO (2–1) velocity channel map of blue bullet 3. Contours levels correspond to $-3, 3, 5, 8, 12, 16,$ and 20σ , then increase in steps of 5σ , where the 1σ level is $\sim 32 \text{ mJy beam}^{-1}$. In each panel, the two crosses mark the peak positions of the dust continuum sources (SVS 13 A and B). The dashed line arrow in each panel shows the overall direction of the SVS 13 A blueshifted jet.

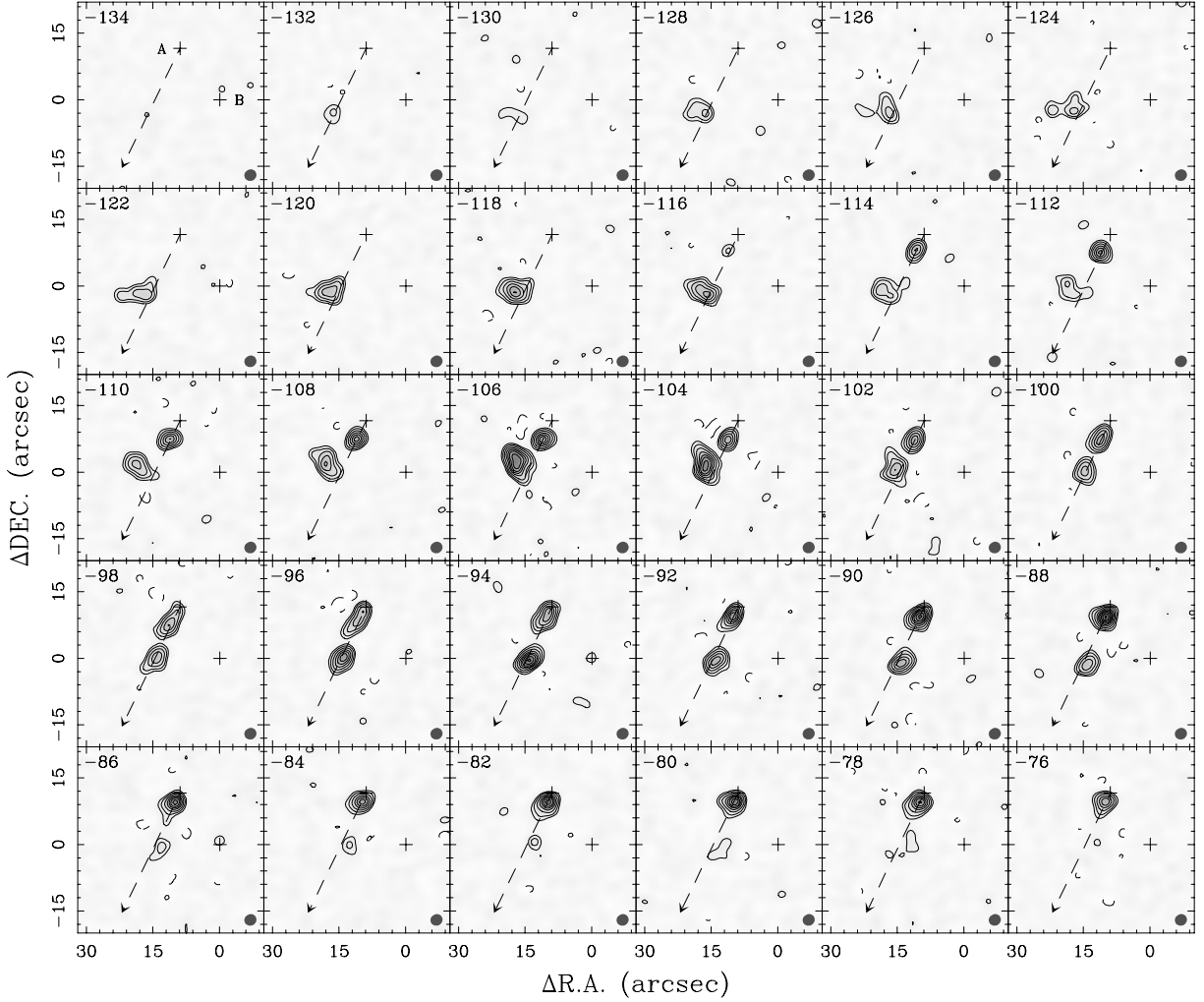


Fig. 8a.— SMA CO (2–1) velocity channel map of blue bullets 2 & 1. Contours levels correspond to $-3, 3, 5, 8, 12, 16,$ and 20σ , then increase in steps of 5σ , where the 1σ level is $\sim 25\text{mJy beam}^{-1}$. In each panel, the two crosses mark the peak positions of the dust continuum sources (SVS 13 A and B). The dashed line arrow in each panel shows the overall direction of the SVS 13 A blueshifted jet.

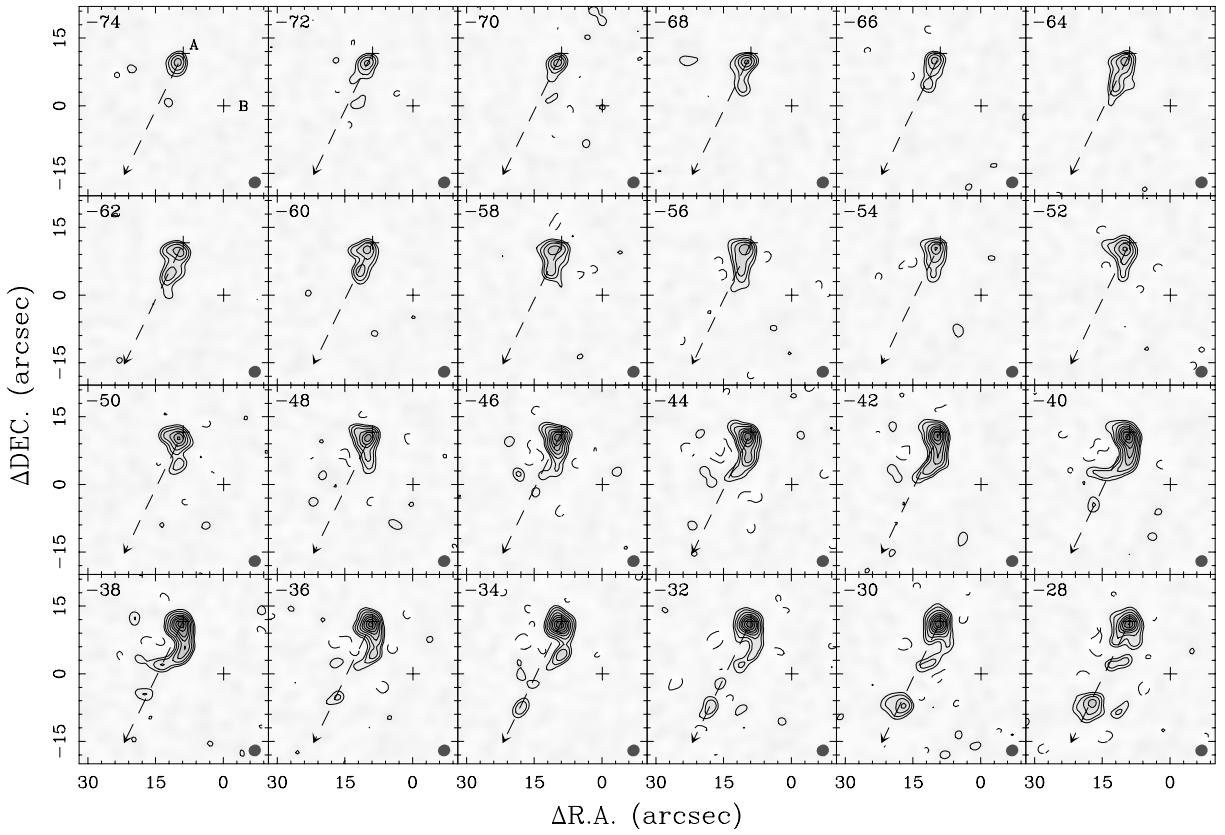


Fig. 8b.— (continued).

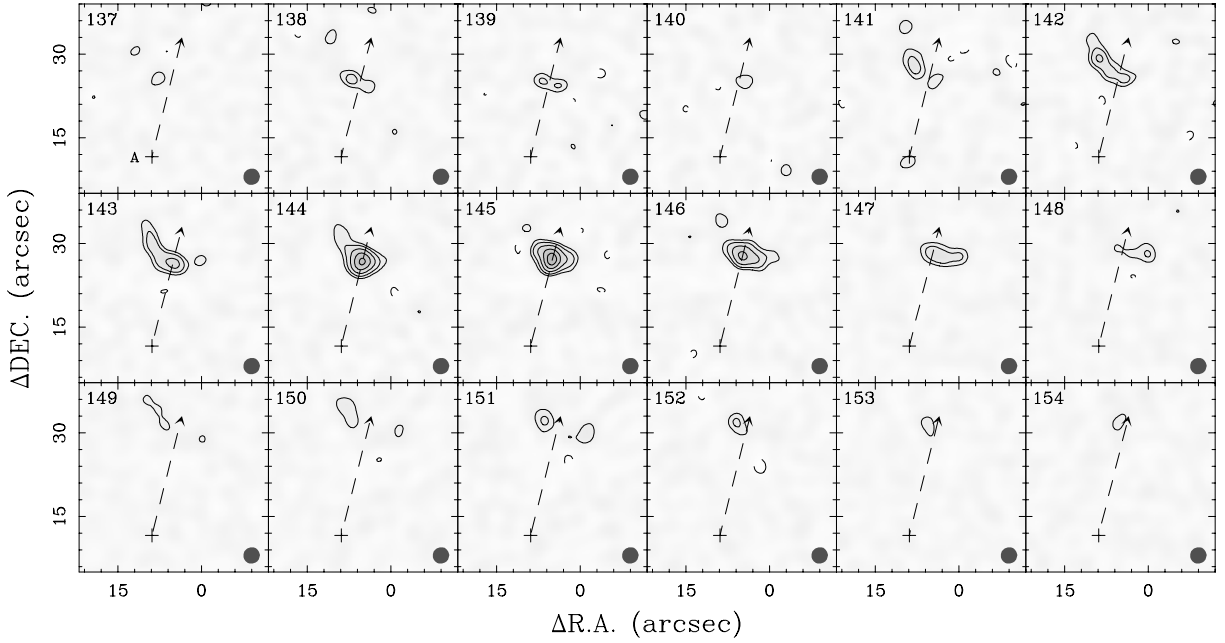


Fig. 9.— SMA CO (2–1) velocity channel map of red bullet. Contours levels correspond to $-3, 3, 5, 8, 12,$ and 16σ , where the 1σ level is $\sim 30 \text{ mJy beam}^{-1}$. In each panel, the cross marks the peak position of the dust continuum source SVS 13 A, while the dashed line arrow shows the direction of the redshifted jet.

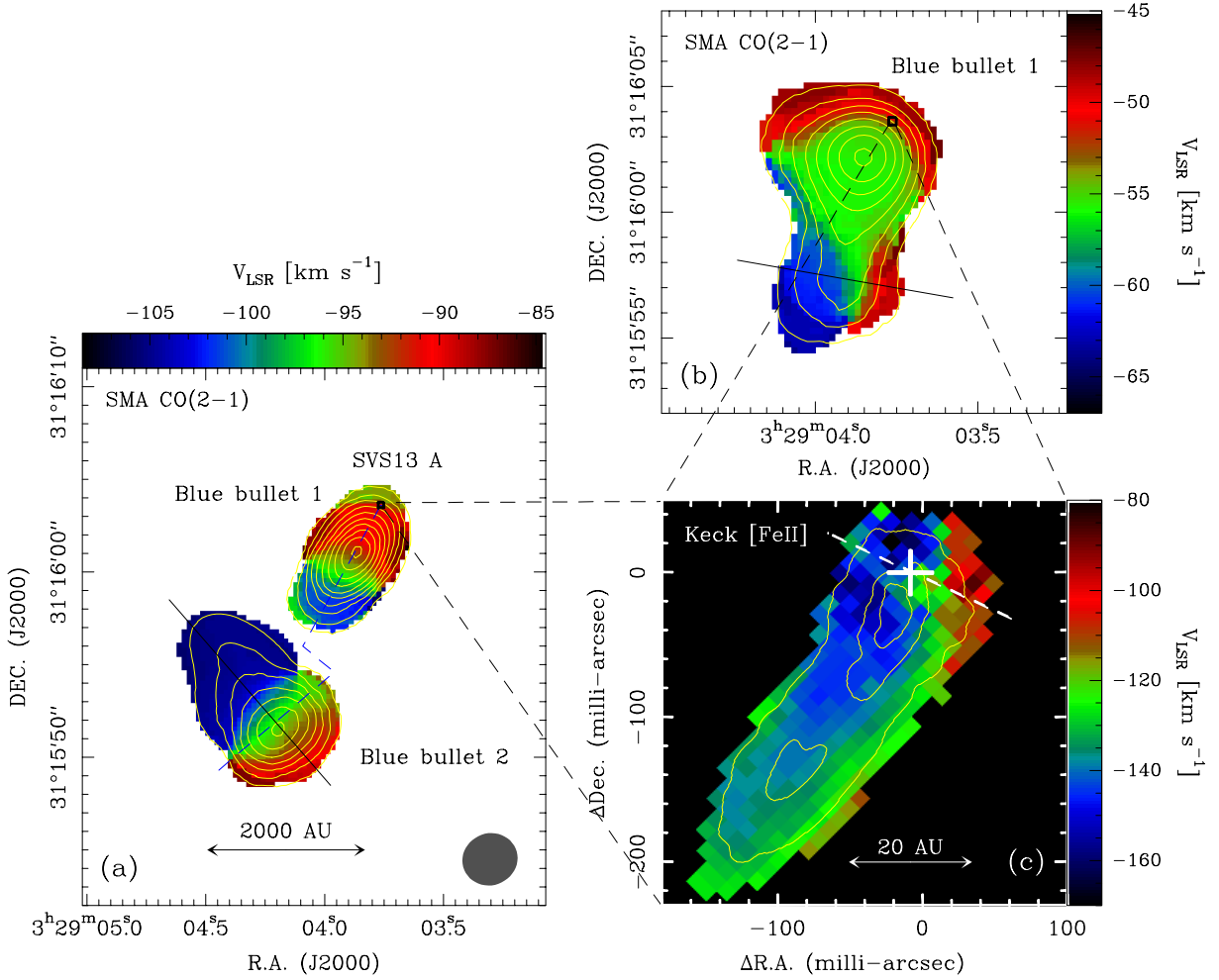


Fig. 10.— (a) SMA CO (2–1) mean velocity field of blue bullets 2 and 1 (1st moment map; from Figure 2). (b) SMA CO (2–1) mean velocity field of the low velocity part of blue bullet 1 (1st moment map; from Figure 5). (c) Velocity map of the continuum-subtracted [Fe II] 1.644 μm data of the SVS 13 microjet, taken with the Keck telescope in 2012 (from Hodapp & Chini 2014). The cross marks the position of the driving source SVS 13 VLA 4B. The white dashed line shows the direction of a tentative velocity gradient across the driving source.

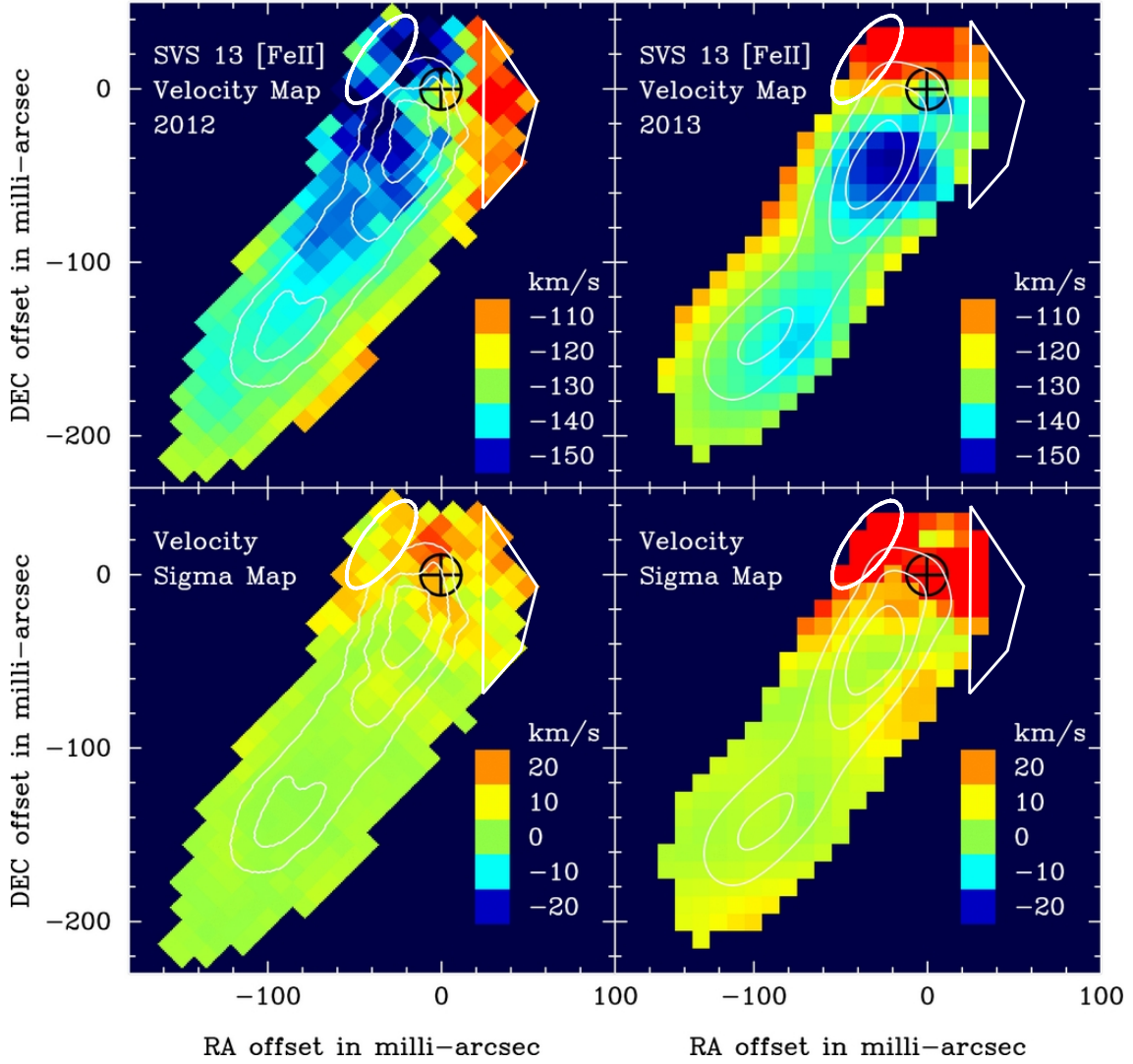


Fig. 11.— The image is adapted from Figure 9 in Hodapp & Chini (2014). Top panels: velocity map of the continuum-subtracted [Fe II] $1.644 \mu\text{m}$ wavelength data cubes of the SVS 13 jet, observed in 2012 and 2013, respectively. The bottom panels show the corresponding velocity sigma maps, showing the rms variations of the velocity measurements on the individual data cubes. The white ellipse and trapezium in each panel mark the same places where a tentative velocity gradient appears in the 2012 data.